Ultrasonics Sonochemistry 82 (2022) 105844

Contents lists available at ScienceDirect

Ultrasonics Sonochemistry

journal homepage: www.elsevier.com/locate/ultson

Collapse pressure measurement of single hollow glass microsphere using single-beam acoustic tweezer

Jinhee Yoo [a,b,1], Hyunhee Kim [b,c,1], Yeonggeun Kim [b,c], Hae Gyun Lim [d,*], Hyung Ham Kim [a,b,c,e,*]

[a] School of Interdisciplinary Bioscience and Bioengineering, Pohang University of Science and Technology, Pohang 37673, Republic of Korea
[b] Medical Device Innovation Center, Pohang University of Science and Technology, Pohang 37673, Republic of Korea
[c] Department of Convergence IT Engineering, Pohang University of Science and Technology, Pohang 37673, Republic of Korea
[d] Department of Biomedical Engineering, Pukyong National University, Busan 48513, Republic of Korea
[e] Department of Electrical Engineering, Pohang University of Science and Technology, Pohang 37673, Republic of Korea

ARTICLE INFO

Keywords:
Collapse pressure
High-frequency ultrasound
Single hollow glass microsphere
Single-beam acoustic tweezer
Acoustic pressure measurement

ABSTRACT

Microbubbles are widely used in medical ultrasound imaging and drug delivery. Many studies have attempted to quantify the collapse pressure of microbubbles using methods that vary depending on the type and population of bubbles and the frequency band of the ultrasound. However, accurate measurement of collapse pressure is difficult as a result of non-acoustic pressure factors generated by physical and chemical reactions such as dissolution, cavitation, and interaction between bubbles. In this study, we developed a method for accurately measuring collapse pressure using only ultrasound pulse acoustic pressure. Under the proposed method, the collapse pressure of a single hollow glass microsphere (HGM) is measured using a high-frequency (20–40 MHz) single-beam acoustic tweezer (SBAT), thereby eliminating the influence of additional factors. Based on these measurements, the collapse pressure is derived as a function of the HGM size using the microspheres' true density. We also developed a method for estimating high-frequency acoustic pressure, whose measurement using current hydrophone equipment is complicated by limitations in the size of the active aperture. By recording the transmit voltage at the moment of collapse and referencing it against the corresponding pressure, it is possible to estimate the acoustic pressure at the given transmit condition. These results of this study suggest a method for quantifying high-frequency acoustic pressure, provide a potential reference for the characterization of bubble collapse pressure, and demonstrate the potential use of acoustic tweezers as a tool for measuring the elastic properties of particles/cells.

1. Introduction

Microbubbles have been thoroughly studied in fields such as medical ultrasound imaging and drug delivery, and their applications can be classified in terms of the mode of use, that is, collapse or non-collapse. The most common use of the non-collapse mode is as an ultrasound contrast agent [1,2]; microbubbles can be used to amplify echo signals during ultrasound imaging by generating a subharmonic response. To maximize the efficiency of the non-inertial cavitation of microbubbles, we need to comprehend the applied pressure to enable the use of the mechanical index as a guide to avoiding microbubble breakage while improving echogenicity [3]. The collapse mode of microbubbles has also been actively investigated in the context of biomedical applications such as nuclei cavitation [4], gene localization, and drug delivery [5,6]. Ultrasound pulses can rupture a cloud of microbubbles to release therapeutic agents at a designated site; however, if the acoustic pressure required to rupture the microbubbles is too high, the heat or cavitation can have adverse side effects [7,8]. The increased risk of cavitation can cause tissue damage even at the relatively low range of mechanical indexes, i.e., $\leq$0.4 [9–11]. Therefore, accurate quantification of the collapse pressure is required for the effective use of microbubbles.

Although the collapse pressure of various bubble types can be

* Corresponding authors at: Department of Convergence IT Engineering, Pohang University of Science and Technology, Pohang 37673, Republic of Korea (H.H. Kim) and Department of Biomedical Engineering, Pukyong National University, Busan 48513, Republic of Korea (H.G. Lim).
E-mail addresses: hglim@pknu.ac.kr (H.G. Lim), david.kim@postech.ac.kr (H.H. Kim).
[1] Equal contribution.

https://doi.org/10.1016/j.ultsonch.2021.105844
Received 12 September 2021; Received in revised form 8 November 2021; Accepted 21 November 2021
Available online 25 November 2021

quantified, accurate measurement is difficult because many bubbles can be easily dissolved in solution or destroyed by cavitation or heat [5,12–15]. Previous studies on collapse pressure disregarded the influence of such external factors; to accurately measure microbubble collapse pressure, the microbubbles should be stable with respect to these factors. Hollow glass microspheres (HGMs) meet these requirements; they are composed of soda-lime-borosilicate glass, which is spherical and hollow, and has a single, thin outer wall (<1 μm thick). They are widely used in non-medical applications such as oil expansion [16], thermal insulation [17], and weight reduction [18]. In the medical field, HGMs are utilized for cell sorting or cell wall destruction owing to their rigidity [19,20]. HGMs do not dissolve and have high collapse pressure and low thermal conductivity [16–18]. Because they are brittle, HGMs produce clear collapse patterns when ruptured. However, compared to other soft-based bubbles, the stiffness of HGM necessitates the use of a high-pressure ultrasound beam to measure the collapse pressure.

Although microbubble-based ultrasound imaging usually requires the use of low frequencies ranging from 1 to 10 MHz, in recent years, many researchers have explored high-frequency applications (>10 MHz). High-frequency imaging using contrast agents is advantageous as this imaging approach can be used to solve the problem of increased attenuation following improved echogenicity and yields more optimized resolution than low-frequency imaging [21–25]. Furthermore, a sharp high-frequency ultrasound beam can deliver genes and drugs to local regions with high precision. High-frequency imaging-based micro-unit studies at the single-cell level are also being conducted [26–28]. However, despite recent growing interest in such applications, studies on high-frequency microbubble dynamics are rare [12]. In addition, the low-frequency mechanics of microbubbles are considered along with their mechanical effects [29–31]. As the likelihood of cavitation is reduced at high frequencies because of the reduced mechanical index, the collapse pressure can be measured more accurately because the acoustic pressure applied to the bubble is the dominant factor that affects the collapse [32]. Likewise, using a frequency that is significantly higher than the resonance frequency can reduce the resonance effect of the bubble, thereby contributing to accurate measurements [33]. Therefore, understanding the high-frequency dynamics of microbubbles is necessary for the study of high-resolution imaging and high-precision enhanced drug delivery.

In addition to cavitation, bubble dynamics factors include size, population, and boundary type, which are usually described using the Rayleigh-Plesset equation [34]. The size of a bubble is inversely proportional to the square of its collapse pressure [35]. The bubble population and boundary type are mechanically important to pressure measurement. To understand the mechanism of bubble collapse, models comprising a single bubble near a rigid wall are widely used because they can be used to specify the impacts of bubble size, population, and boundary effects in a well-defined setting [36–39]. Models involving multiple bubbles have also been used to observe changes in natural frequency and collapse pressure [40–42], which are dependent on the interactions and void fractions between bubbles [43–46]. Such models must solve for more variables than single-bubble models and determine the collapse pressure based on the surrounding environment rather than the dynamics and structure of the bubble itself. Therefore, a single-bubble response is more suitable for measuring the collapse pressure of bubbles because the associated dynamics are less affected by the surrounding environment.

Passive cavitation detection is the preferred approach for measuring the collapse pressure of microbubbles [12,15,47–50]. Under this approach, collapse pressure is measured by applying an acoustic beam to a bubble and detecting the signal that occurs when the bubble ruptures. However, this is very challenging for single bubble measurement owing to the need to confirm that the signal is produced by exactly one bubble, which can be done by measuring the distance to the bubble or the shape of the received signal [47–49]. Another significant limitation of passive cavitation detection is that it indirectly measures the collapse pressure, which limits the accuracy of its results. Current solutions include statistical methods [49,50] and measurement using static overpressure [51,52].

Non-contact particle trapping techniques such as acoustic or optical tweezers are a robust potential tool for studying single microbubble dynamics [53,54]. Tweezer approaches can be used to trap a single microbubble from a bubble cloud by isolating the bubble using a focused beam while pushing the surrounding bubbles away. Optical tweezers have high spatial resolutions, enabling precise particle collection and selection [55,56]. However, optical tweezers have the critical drawback of generating excessive heat, which has a thermal effect on the particle and affects the collapse pressure of the bubble [9,37,57]. More significantly, because the trapping and radiation forces of optical tweezers are limited to the pico-Newton (10^{-12}N) range [58–61], they are not suitable for rupturing microbubbles. Acoustic tweezers, by contrast, are free from such photothermal effects [62,63] and can generate strong trapping forces at the nano-Newton (10^{-9}N) level [64]. This nN-scale trapping force ensures stable trapping even at high pressure levels within the range of a few MPa and is robust against external forces. There are many types of acoustic tweezers, including approaches based on the use of surface acoustic [65,66] or traveling waves [67] and potential wells [68]. Of these, single-beam acoustic tweezers (SBATs) [58,62–64,69–71] can trap particles using a single transducer, enabling the selective trapping of either single or multiple particles depending on the particle size and beamwidth. In addition, SBATs do not require complex implementation setups [58,69]. There are many microbubbles or cell studies that require micrometer-level displacement control and substantial trapping force, and high-frequency (>10 MHz) SBAT is potentially the optimal approach toward studying micrometer-sized bubbles because it satisfies the requirements of such studies.

In this study, we developed a method for measuring the collapse pressure of a single HGM using a high-frequency SBAT. To the best of our knowledge, acoustic tweezing to measure microsphere collapse has not been applied in any previous studies. We chose a HGM as the research target because the solid shells of these structures are less affected by external factors and their properties can be more accurately quantified than those of other microbubbles. The proposed approach uses a frequency range of 20–40 MHz to avoid cavitation and resonance. Since it is difficult to measure acoustic pressure using higher frequencies, we chose the frequencies as high as possible (20, 25 MHz) and twice as high (40 MHz). In addition, single microsphere trapping was made possible by the use of a relatively small beamwidth (due to higher frequency) to rule out interactions between microspheres. SBAT has enough force to reliably trap the HGM and completely rupture it. Under these controlled conditions, we measured the collapse pressure of a HGM based on the acoustic pressure at the given transmit condition, which was characterized by the hydrophone measurements. Measurements of the collapse pressures at 20 and 25 MHz demonstrated that the frequency did not affect the collapse pressure. To apply the proposed method to smaller microspheres, a 40 MHz high-frequency transducer was used. Because measuring acoustic pressure using hydrophone when a 40 MHz transducer is used is difficult, the collapse pressure of the 34–48-μm microsphere was indirectly measured using a derived collapse pressure estimation curve. The curve was further used to identify the acoustic pressure characteristics of the 40 MHz transducer. Advantage of the technique demonstrated in this paper is that it can compensate for the limitations of the current hydrophone technology by allowing for high-frequency measurements with beam sizes that are smaller than the aperture size of a needle hydrophone (the minimum sizes is typically 40 μm). Furthermore, this study was conducted with HGM for accuracy, but if a higher-frequency transducer were to be fabricated, this technique could be used to measure the collapse pressure of smaller contrast agents ranging from 1 to 10 μm in size or air bubbles in water.

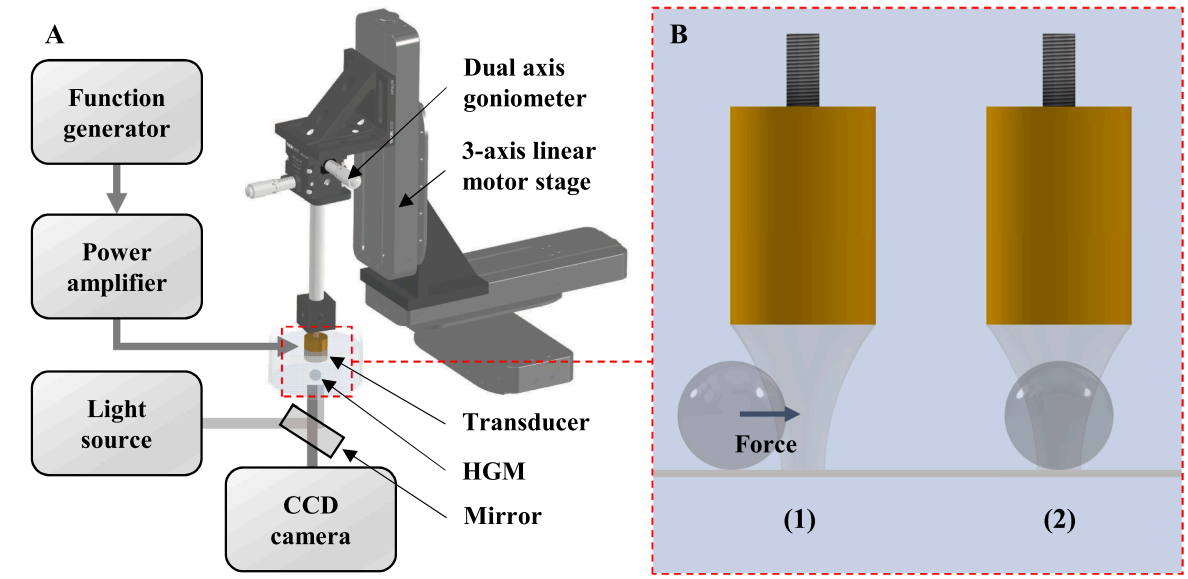

Fig. 1. Schematic of collapse pressure measurement system. (A) Overall schematic. The system is divided into ultrasound radiation (function generator – transducer), microsphere imaging (light source – CCD camera), transducer alignment, and position control (dual-axis goniometer, 3-axis linear motor stage) components. (B) Magnified schematic of ultrasound radiation component of SBAT setup sequence. Ultrasound radiation near a HGM traps it at the focal point of the ultrasound transducer.

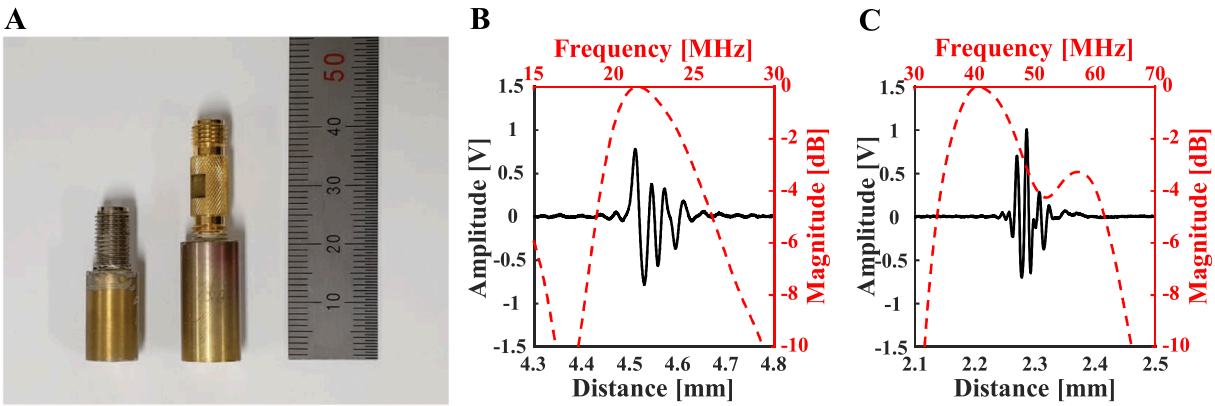

Fig. 2. Properties of ultrasound transducers used as SBATs. (A) Image of the fabricated transducers. (B) Pulse echo response with a center frequency of 23 MHz and a bandwidth of 35% based on −6 dB. (C) Pulse echo response with a center frequency of 48 MHz and a bandwidth of 62% based on −6 dB.

2. Experimental setup

2.1. Acoustic tweezers for particle manipulation

An acoustic tweezer microscope system to trap and manipulate HGMs was formed using an SBAT with a five-axis control and an inverted microscope was used to observe the rupture process (Fig. 1). The signal generated by a function generator (SG382, Stanford Research Systems, Sunnyvale, CA, USA) was amplified using a power amplifier (525LA, Electronics & Innovation, Ltd., Rochester, NY, USA) and applied to the transducer. The X-, Y-, and Z-coordinates of the SBAT were controlled using a linear motorized stage (OSMS20-85, Sigma Koki Co., Ltd, Tokyo, Japan) and the θ and Φ angles were controlled using a dual-axis goniometer (GNL 20/M, Thorlab Inc., Newton, NJ, USA). An inverted microscope (IX-73, Olympus, Center Valley, PA, USA) was used to observe the motion and breakage of the HGMs, which were recorded using a CMOS camera (ORCA-Flash4.0 V3, Hamamatsu Photonics, Shizuoka, Japan) and imaging software (MetaMorph, Molecular Devices, LLC, San Jose, CA, USA).

A Petri dish containing deionized water was placed in the acoustic tweezer system and the SBAT transducer was immersed in water and manipulated using the linear motorized stage system. The transducer was excited by pulses generated by a pulser-receiver (DPR500, Imaginant Inc., Pittsford, NY, USA) and the position of the transducer was adjusted by observing the echo to place the focal point at the bottom surface of the Petri dish. HGMs (Glass bubbles K15, 3M, Maplewood, MN, USA) were then placed in the Petri dish (Fig. 1B-1). To trap HGMs, the SBAT was driven by square wave with a peak-to-peak voltage (V_{pp}) of 3 V, a pulse repetition time of 1 ms, and a duty factor of 1% (Fig. 1B-2). HGMs of various sizes were used because the size of the microspheres trapped by acoustic tweezers can depend on the frequency and beamwidth [69,72].

2.2. Transducers for single-beam acoustic tweezer (SBAT)

Two ultrasound transducers were fabricated for the SBAT (Fig. 2A). Each transducer was designed using Krimholtz, Leedom, and Matthaei (KLM) model-based software (PiezoCAD, Sonic Concepts, Bothell, WA, USA). In general, SBAT transducers require highly focused beams that can be formed with high frequencies and low f-numbers [63]. For the fabrication of the high-frequency SBAT, a 36° rotating Y-shaped lithium niobate (Boston Piezo-Optics Inc, Bellingham, MA, USA) was used as a

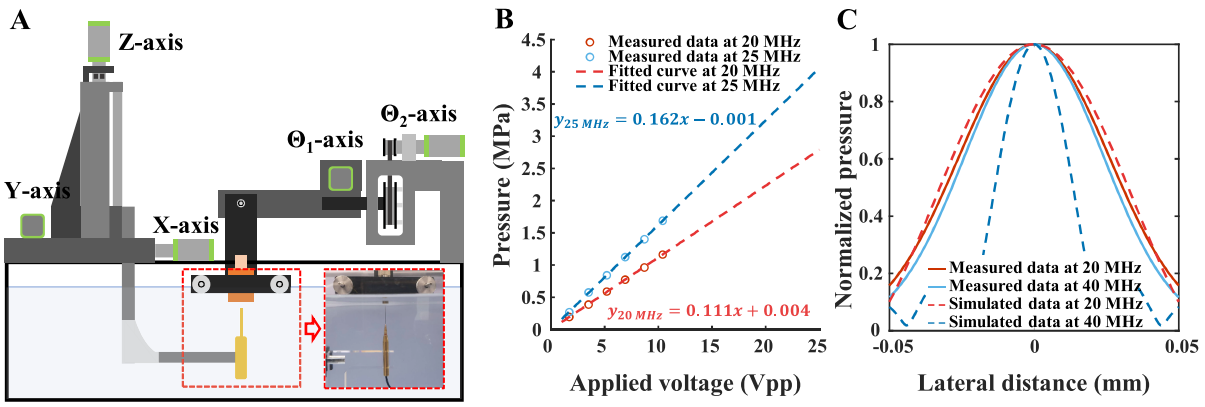

Fig. 3. Acoustic pressure characteristics of ultrasound transducers. (A) Schematic of transducer acoustic pressure measurement using a hydrophone (green markings indicate motor). (B) Acoustic pressure measurement and fitted results at applied voltages of 1.7, 3.6, 5.2, 6.9, 8.7, and 10.4 V_{pp}. The data obtained at 20 and 25 MHz are fitted to linear regressions, with both obtaining $R^2 > 0.999$. (C) Lateral resolution measurement and simulation results. Measured data at 20 and 40 MHz are fitted with a Gaussian model and obtain $R^2 = 0.970$ and 0.997, respectively.

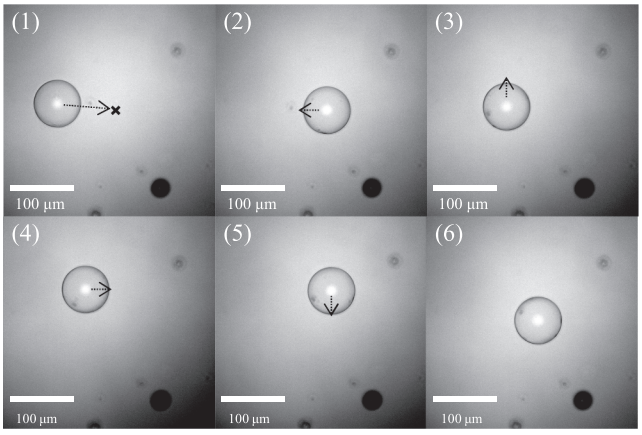

Fig. 4. HGM trapped by SBAT at 20 MHz. Trapping is evaluated by moving the transducer with a linear motor. HGM (1) moving freely before being trapped at the focal point. Trapped microsphere (2) moving to the left, (3) upward, (4) to the right, and (5) down. The size of the HGM is 73 μm.

piezo material. Lithium niobate has a piezoelectric performance comparable to that of zirconate titanate (PZT) and a low dielectric constant, which can be useful for fabricating a high-frequency transducer with a large aperture. The proposed device achieves low f-numbers by press-focusing the entire aperture of the lithium niobate piece to form a tight beam shape. The impulse response of each transducer was measured using a pulser-receiver (Fig. 2B, C). The −6 dB center frequencies of the two transducers were 23 MHz and 48 MHz, and their f-numbers 0.75 and 0.55.

2.3. Measurement of acoustic pressure

A beam-profile test system (IPB760, IMP Systems, Gyeongsangbuk-do, South Korea) and hydrophone (NH0040, Precision Acoustics, Dorchester, UK) were used to measure the acoustic pressure characteristics of the transducers. The five-axis beam profile test system was used to move the hydrophone along the X-, Y-, and Z-axes and to adjust the transducer along the θ and Φ axes (Fig. 3A). After mounting the transducer and hydrophone onto the test system, 3D alignment was performed. Acoustic pressure was measured by increasing the applied voltage at the position in 3D space at which the pressure was highest. As hydrophones cannot measure high acoustic pressures above 10 MPa, such measurements must be made at low applied voltages; however, because the applied voltage and output acoustic pressure have a linear relationship, the characteristics of higher applied voltages could be determined by first-order linear fitting (Fig. 3B). The acoustic pressure characteristics of the 23 MHz center-frequency transducer were measured at frequencies of 20 and 25 MHz, which had sufficient pulse-echo responses despite not coinciding with the center frequency (Fig. 2B). The measurements revealed that the acoustic pressure measured at 25 MHz was higher than that measured at 20 MHz at a given applied voltage. A comparison between the efficiencies at 20 and 25 MHz is given in Section 3.d.

The lateral resolution was measured as the acoustic pressure relative to position by scanning along the X-or Y-axes from the positions at which the pressure was highest at given depths. The lateral resolutions at 20 and 40 MHz were measured using 23 and 48 MHz transducers, respectively; in a manner similar to the acoustic pressure characteristic measurements, we used frequencies with sufficient amplitudes to obtain pulse-echo responses rather than the center frequency (Fig. 2B, C). Generally, the lateral resolution should be inversely proportional to the frequency. However, our measurement results revealed nearly no change in the lateral resolution between 20 and 40 MHz. More specifically, the full half-width maximum (FWHM) of the measured lateral resolutions were 60 and 57 μm at 20 and 40 MHz, respectively, and the simulated lateral resolutions obtained using Field II [73] were 65 and 27 μm at 20 and 40 MHz, respectively. Considering that the calculated lateral resolutions at 20 and 40 MHz were 56 and 21 μm, respectively, we found a large error in the measurement result at 40 MHz (calculated lateral resolution = f-number × wavelength) owing to the spatial averaging effect [74–76]. If the effective diameter of the hydrophone is larger than the lateral resolution, the measured parameters are affected by spatial averaging. Specifically, for 20 and 25 MHz, the effective diameter of the hydrophone that we used, 40 μm, was smaller than the lateral resolution of 20 and 25 MHz, so the acoustic pressure could be measured correctly. However, for 40 MHz, the effective diameter was larger than the lateral resolution, so the acoustic pressure was not measured correctly. To address this issue, we carried out an indirect measurement of acoustic pressure using high-frequency transducers following the procedures described in detail in Section 3.f.

2.4. Measurement of the collapse pressure of HGMs

The collapse pressures of HGMs were measured by recording the applied voltage on the SBAT transducer during the collapses of single HGMs trapped by the acoustic tweezer. During trapping, the diameters of the microspheres were accurately measured using a microscopic ruler (minimum scale = 1 μm). Because the microspheres wobbled at high applied voltages and escaped trapping at low applied voltages, an initial input voltage of 3 V_{pp} was applied based on optimization across all

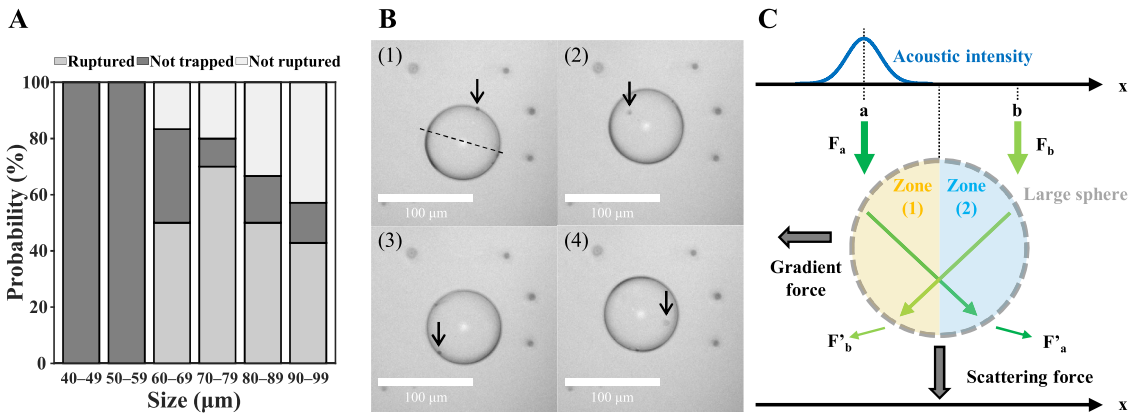

Fig. 5. Measurable range and basis for collapse pressure at 20 MHz. (A) Probability of measuring collapse pressure according to microsphere size (measurements obtained for n = 8, 10, 6, 10, 6, and 7 microspheres in respective groups of increasing size). The results are divided into three types: ruptured, not trapped, and not ruptured. (B) Image of trapped-but-not-ruptured case, where the microsphere engages solely in rolling; microsphere size is 79 μm. (C) Schematic of SBAT mechanism application to large sphere obtained using the ray approach.

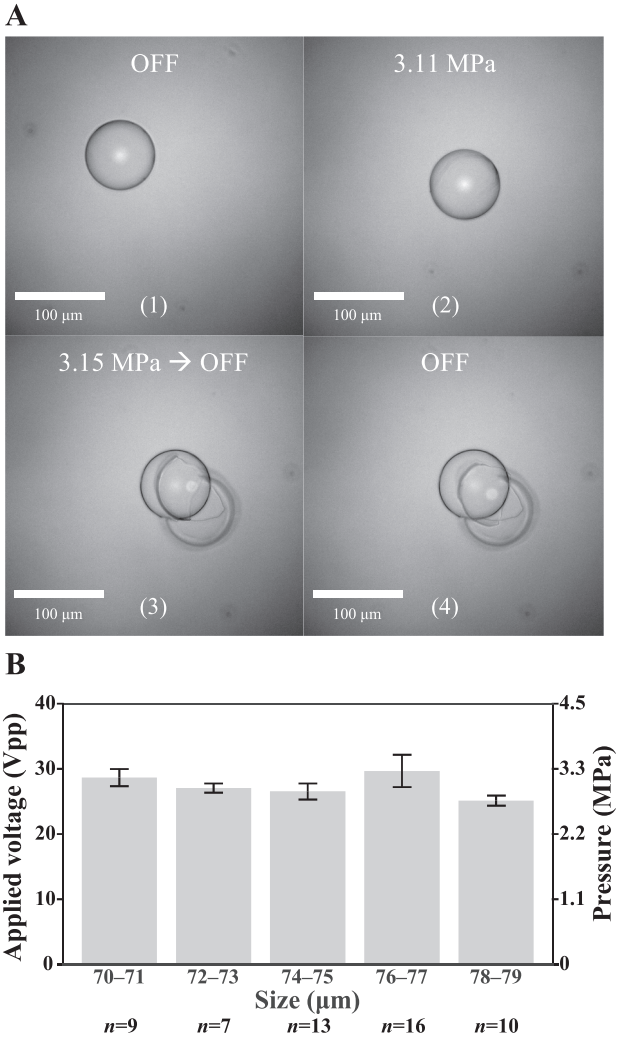

Fig. 6. Measurement of collapse pressure at 20 MHz. (A) Increase in acoustic pressure over time leading to microsphere collapse; microsphere size, 76 μm. (B) Threshold applied voltage and acoustic pressure by microsphere size obtained for n = 9, 7, 13, 16, and 10 microspheres in respective size groups. Results of one-way analysis of variance (ANOVA) test, P = 0.443. Bar graph represents mean ± s.e.m.

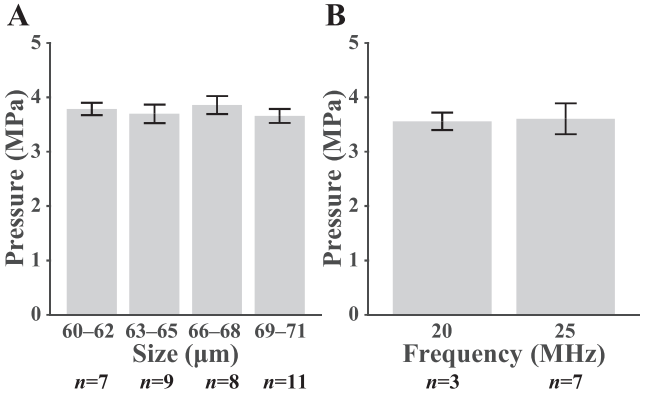

Fig. 7. Measured collapse pressures at 25 MHz and comparison with 20-MHz results. (A) Threshold data for acoustic pressure as a function of microsphere size at 25 MHz (one-way ANOVA, P = 0.804). (B) Threshold data for acoustic pressure for 70-μm microspheres at 20 and 25 MHz (two-tailed *t*-test assuming equal variance, P = 0.893). All bar graphs represent mean ± s.e.m.

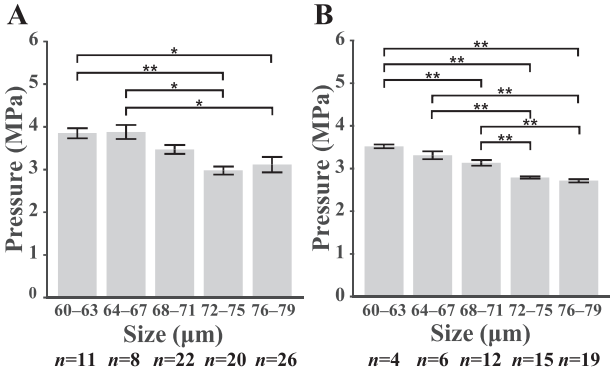

Fig. 8. Collapse pressure as a function of microsphere size at 20 and 25 MHz. (A) Threshold data for acoustic pressure according to microsphere size at 20 and 25 MHz (one-way ANOVA with a Tukey honestly significant difference post hoc test, $P = 4 \times 10^{-4}$; details for each group are listed in Table S1). (B) Primary threshold data for acoustic pressure by microsphere size at 20 and 25 MHz (one-way ANOVA with a Tukey honestly significant difference post hoc test, P < 0.001; details of each group are listed in Table S2). All bar graphs represent mean ± s.e.m. *P < 0.05, **P < 0.01.

Table 1
Calculated Young's modulus and radius ratio.

HGM size (μm)	Collapse pressure (MPa)	True density (g/cc)	HGM thickness (μm)	Young's modulus (GPa)	Radius ratio
61.5	3.523	0.150	0.689	5.958	0.978

frequency bands and the applied voltage was increased by approximately 0.2 V_{pp} per second until the trapped microspheres ruptured. At the moment of rupture, the applied voltage was recorded and converted to acoustic pressure based on the hydrophone measurement, and the acoustic pressure was expressed as the collapse pressure of the ruptured HGM. Fifty-five, thirty-five, and forty-eight HGMs were measured at 20, 25, and 40 MHz, respectively. Error bars are presented as mean ± standard error of the mean (s.e.m.). The procedures used in the measurement process are described in detail in Section 3.c.

3. Results and discussion

3.1. HGM trapping

Single HGMs were trapped at the focus of the ultrasound beam generated by a 20 MHz SBAT (Fig. 4, Video S1) and moved along the path of mechanical translation of the tweezer transducer (Fig. 1). Before applying the ultrasound field, the HGMs moved freely (Fig. 4-1); when the acoustic tweezer was turned on, they were trapped at the focal point (Fig. 4-2). As the transducer moved left, up, right, and down, the trapped HGM moved along with the transducer (Fig. 4-2–4-6) without affecting the other microspheres in the surrounding area. We observed the same trapping pattern when moving the Petri dish (Video S1) while keeping the acoustic tweezer still.

3.2. Finding the size range of microspheres to measure the collapse pressure

There were two cases where pressure measurement was not possible: when the microspheres could not be trapped and when they did not rupture. Using SBAT at 20 MHz, the collapse pressures of microspheres of various sizes were measured to determine acceptable ranges for trapping and rupturing (Fig. 5A). Theoretically, an SBAT can trap particles larger than its beamwidth through a phenomenon that can be described using the ray approach, but it cannot trap particles similar in size to its beamwidth [68,69]. We were unable to trap HGMs ranging from 40 to 59-μm in size because the lateral resolution of ultrasound at 20 MHz of 60 μm was similar in size to the microspheres. We also found that increasing the microsphere size increased the probability of trapping without rupture. Based on these results, we concluded that the collapse pressure measurement of 60–99-μm diameter microspheres is possible at 20 MHz but that the best measurement results can be obtained in the 70–79-μm range, which was approximately 15 μm larger than the lateral resolution (Fig. 5A).

We then compared the differences between the behavior of ruptured and unruptured microspheres. Whereas the unruptured microspheres rotated along an axis parallel to the floor (Fig. 5B, Video S2), the ruptured microspheres rotated along an axis perpendicular to the floor (Videos S3 and S4). The particle rotation mechanism of acoustic tweezers is not well known and, to better understand this phenomenon, we analyzed the particle rotation mechanism of the optical tweezers using the ray approach [59,77]. Under optical tweezing, the direction of rotation can be divided into yaw, pitch, and roll components. In our results, the unruptured and ruptured microspheres rotated approximately along the pitch and yaw directions, respectively. Although pitch rotation is associated with asymmetric spherical particles, the asymmetric application of ultrasonic waves to sufficiently large symmetric HGMs would also be expected to induce pitch rotation. To examine this, we considered the case of a HGM located at a point on the x-axis with the ultrasound focused at the point " a " (Fig. 5C). If the diameter of the HGM (d) is significantly larger than the beamwidth ($\lambda \ll d$), the conventional ray approach is not applicable and the area inside the HGM can be divided into two zones: zone 1 (near the focus, yellow-colored), where the ultrasound force (F_a) is strong; and zone 2 (away from the focus, magenta-colored), where F_b converges to zero . The conventional ray approach, which assumes that both F_a and F_b affect the particle along a beam profile of Gaussian intensity, alters the particle's momentum by a net force consisting of the incident (F_a , F_b) and refractive forces ($F_a^{'}$, $F_b^{'}$). However, in this case, as the magnitude of F_b has no effect on the HGM, force asymmetry occurs in each zone, creating torque and causing the HGM to roll, making it difficult to rupture.

3.3. Collapse pressure measurements at 20 MHz

We trapped HGMs and then gradually increased the applied voltage to the acoustic tweezer until rupture occurred (Fig. 6A). While increasing the applied voltage, we transversely manipulated in the vertical direction of the ultrasound beam to confirm that they were trapped. Upon reaching a specific pressure, cracks or partial ruptures occur (Fig. 6A-2). When the microspheres ruptured, the ultrasound radiation was halted, and the applied voltage was recorded (Fig. 6A-3). The HGM completely ruptures into two pieces (Fig. 6A-4). To obtain the collapse pressures, the recorded voltages were converted to acoustic pressures based on hydrophone measurements. The recorded HGM size

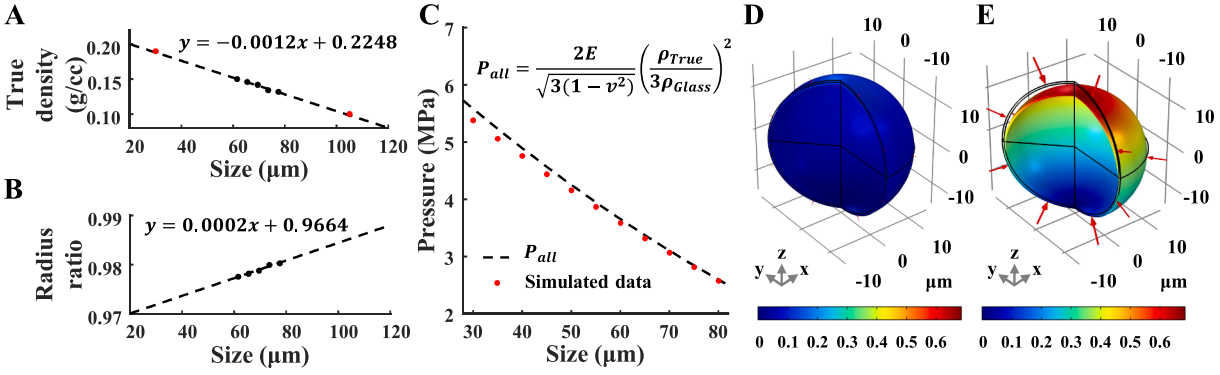

Fig. 9. Characterization and pressure estimation by individual HGM sizes. (A) True density as a function of size fitted with linear regression ($R^2 = 0.974$). Red marks are values estimated from information provided by the manufacturer. (B) Radius ratio as a function of size fitted with linear regression ($R^2 = 0.974$). (C) Collapse pressure characteristics across overall range of HGM sizes. The red marks are the values obtained from the simulation. (D) Simulation result for the displacement of microsphere at 1 MPa. (E) Simulation result for the displacement of microsphere at 5.38 MPa. A stationary study was used in 2D axisymmetric, and the parameters referred to Table S5 (total number of elements = 170, degrees of freedom = 1010).

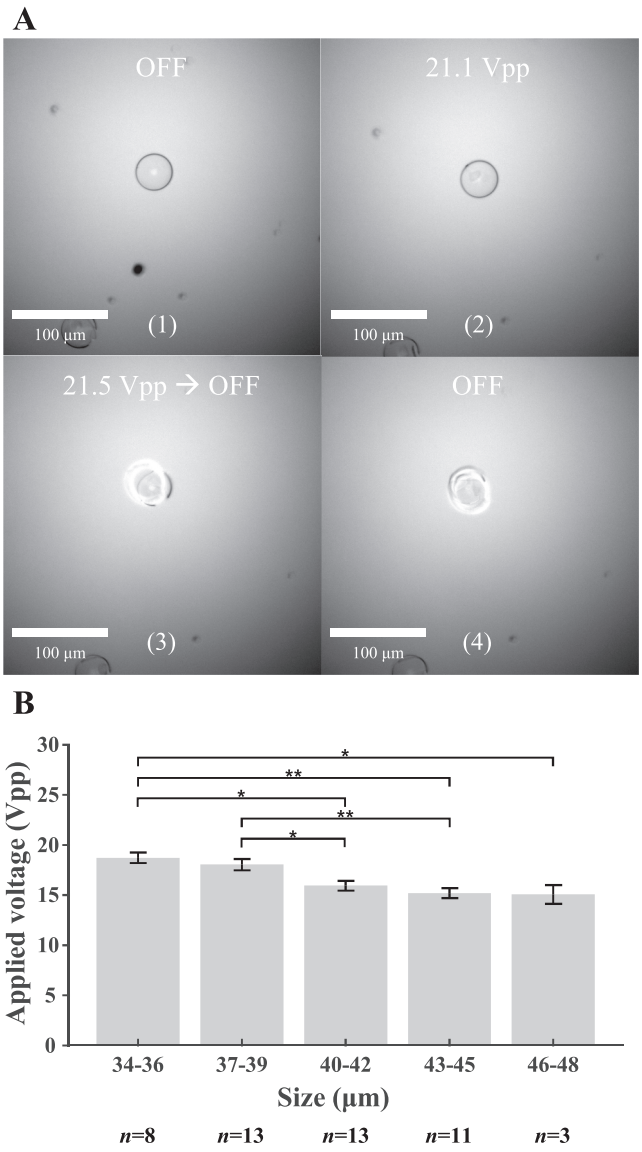

Fig. 10. Measured collapse pressures at 40 MHz. (A) Increase in acoustic pressure over time leading to microsphere collapse; microsphere size, 38 μm. (B) Threshold applied voltage data according to microsphere size. Measurements obtained from groups of n = 8, 13, 13, 11, and 3 microspheres in increasing order of size (one-way ANOVA with a Tukey honestly significant difference post hoc test, $P < 0.001$; details of each group are listed in Table S3). Bar graph represents mean ± s.e.m. *$P < 0.05$, **$P < 0.01$.

was 76 μm and the collapse pressure was 3.15 MPa (Video S2). The degree of cracking and rupture of each HGM was evaluated qualitatively (Fig. S1).

Additional measurements were performed on 55 HGMs ranging from 70 to 79 μm in size (Fig. 6B). A one-way analysis of variance analysis (ANOVA) of the results revealed that there was no significant relationship between the microsphere size and the collapse pressure in this size range, indicating that the collapse pressure of the 70–79-μm microspheres could be assumed to be approximately 3.08 MPa (on average), which exceeds the manufacturer-specified 2.07 MPa. The measured values can vary depending on the collapse pressure measurement method used; in this case, the manufacturer used static pressure whereas the proposed method uses acoustic pressure with both compression and rarefaction. Because the threshold pressure is attained instantaneously, it is measured as a rather high collapse pressure, a result supported by previous studies [5,52,78]. In addition, the manufacturer's criteria for

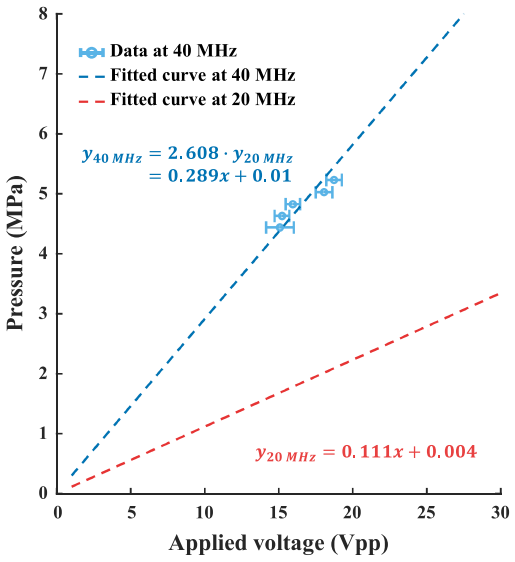

Fig. 11. Expected acoustic pressure characteristics of a 40 MHz transducer. The threshold applied voltage data by size (Fig. 10B) and estimated pressure results by size (P_{all}, Fig. 9C) were used to obtain the estimated data. The 40-MHz data are fitted with a linear regression ($R^2 = 0.551$).

microsphere collapse were based on the 80–90% survival rate of multiple microspheres; conversely, the proposed method observes the moment at which a single microsphere ruptures in real time, enabling a more accurate measurement of collapse pressure than could be obtained by the manufacturer.

3.4. Collapse pressure measurements at 25 MHz

To validate the applicability of the proposed approach at higher frequencies, the collapse pressures at 25 MHz were measured following the same procedure and using the same transducer as that used at 20 MHz. The collapse pressures were also measured over a wide range of microsphere sizes. O'Neil et al. [79] derived the following formula for the acoustic pressure produced by a focused transducer: [80]

$$p = \frac{\rho c u e^{-i\omega t}}{1 - \frac{d}{a}}\left(e^{ikd} - e^{ikR}\right) \quad (1)$$

$$R = a\sqrt{1 + (1 - d/a)^2 - 2\left(1 - \frac{d}{a}\right)\cos\alpha} \quad (2)$$

where ρ and c are the density and speed of sound of the medium, respectively, u is the normal velocity amplitude of the transducer surface, ω is the angular frequency, k is the wavenumber, d is the focal length, and a and α are the radius of the transducer surface and its half-aperture angle, respectively. Because we used the same transducer in a single environment containing hydrophones, ρ, c, d, a, and R were the same at both 20 and 25 MHz and the pressure was solely determined by u, k, and ω, i.e., the pressure was solely influenced by frequency-dependent parameters and unaffected by geometric parameters. If transducers with different f-numbers or apertures of different sizes are used in this analysis, the attenuation or spatial averaging effect should be considered.

We first searched for the range of appropriate microsphere sizes at 25 MHz. To ensure that the measured microsphere size range overlapped with the data at 20 MHz (70–79 μm) for the purpose of continuity and that the sizes exceeded the lateral resolution (45 μm), we selected a range of 60–71 μm (Fig. 7A), which was approximately 15 μm larger than the lateral resolution. Application of a one-way ANOVA to the results for 35 HGMs revealed that the relationship between microsphere

size and threshold pressure was not significant in this range, indicating that the HGM collapse pressure was approximately 3.74 MPa (average value) over the 60–71-μm size range.

The collapse pressure at 25 MHz was 0.66 MPa higher than that at 20 MHz (3.08 MPa). Although the relationship between size and collapse pressure was not significant over either small size range, a significant difference was observed between these results. Two controlled variables—frequency and microsphere size—were available for comparing the results obtained at 25 and 20 MHz. We investigated whether the frequency affected the collapse pressure by measuring the collapse pressures on 70-μm microspheres at 20 and 25 MHz (Fig. 7B). The results of a two-tailed *t*-test assuming equal variance revealed that the ultrasound frequency did not affect the measured collapse pressure. We also calculated the resonance frequency depending on the HGM size and the ratio of amplitude of oscillation depending on the frequency to see the resonance effect with frequency [33,81]. The resonance frequency of 65 μm HGM is 4.37 MHz, and the driving frequency (25 MHz) is approximately 5 times higher, so the resonance with frequency has little effect (Fig. S3). These results indicate that the frequency did not affect the HGM collapse pressure. Therefore, our results revealed that the collapse pressure of a HGM could be measured at 25 MHz and that the microsphere size did not affect the collapse pressure at either 20 or 25 MHz; instead, the disparity in measurements obtained at each frequency indicate that the collapse pressure was size-dependent.

3.5. Collapse pressure characteristics at all HGM sizes

To understand the significant differences in the results obtained at each frequency, we reviewed all results obtained at 20 and 25 MHz (Fig. 8A) and found based on ANOVA testing that the relationship between microsphere size and threshold pressure was significant. To clearly visualize this slight dependency between the two, we classified microsphere collapse pressure into two groups with outliers excluded following the statistical procedures used in previous studies [51]. Using a Gaussian mixed model, we divided the collapses into primary and secondary groups (Fig. S2). Considering that the primary group was more representative of the relationship between collapse pressure and size, we used only this group to confirm the results at 20 and 25 MHz (Fig. 8B). Our ANOVA results revealed that the relationship between size and collapse pressure was more significant for this group, for which it was evident that the collapse pressure increases as the microsphere size decreases.

To explain the phenomenon where the collapse pressure increases as the microsphere size decreases, we used primary group data to determine the factors that affect collapse pressure. The collapse pressure was calculated as follows [35]:

$$\mathrm{P} = \frac{2E}{\sqrt{3(1-\nu^2)}}\left(\frac{2t}{d}\right)^2 \tag{3}$$

where E is Young's modulus, ν is Poisson's ratio, d is the diameter of the microsphere, and t is the thickness of the microsphere. Because Young's modulus and Poisson's ratio are both related to material properties, the variables that determine the collapse pressure are the size and thickness of the microsphere. However, in previous studies the size and thickness of the microspheres were considered together as the radius ratio [82,83], which is given as

$$\eta = 1 - \frac{2t}{d} \tag{4}$$

In previous studies [82,83], the radius ratio of the material used was 0.98 and, therefore, the collapse pressure was constant regardless of size, producing values that were inconsistent with the experimental results of this study. In contrast, some studies where HGMs were measured with a scanning electron microscope (SEM) have shown that the radius ratio is proportional to the microsphere size [84], suggesting that the collapse pressure is dependent on microsphere size and is not constant. We therefore used a radius ratio that varied slightly with size. By using Poisson's ratio of glass in Eq. (3) (0.19), the microsphere size can be measured and the thickness of the microsphere can be calculated [78] as follows:

$$t = \frac{d \bullet \rho_{true}}{6 \bullet \rho_{glass}} \tag{5}$$

where ρ_{true} is the true density (0.15 g/cc, from the data provided by the manufacturer) and ρ_{glass} is the density of borosilicate glass (2.23 g/cc) [78]. The microsphere size was set to be similar to the average sizes in the data provided by the manufacturer, and the collapse pressure was obtained from the primary group at 25 MHz; these data were used to determine the Young's modulus of the HGMs from Eq. (3) as 5.958 GPa and the radius ratio from Eq. (4) as 0.978 (Table 1). These values are similar to the Young's modulus (5.539 GPa) and radius ratio (0.98) for HGMs obtained in previous studies [82,83,85].

Based on the obtained Young's modulus value, the thickness of a microsphere can be calculated as a function of size. Using the collapse pressures obtained from the primary data measured at 20 and 25 MHz and the Young's modulus obtained as shown above, the thicknesses were calculated using Eq. (3) (Table S4), with the results indicating that the true density and radius ratio are inversely and directly proportional to the size, respectively (Fig. 9A, B). The high coefficient of determination (R^2) suggests that the collapse pressure increases as the microsphere size decreases. According to the HGM manufacturer, 10% distribution of spheres are at the size of 30 μm, 50% at 60 μm, and 90% at 105 μm, and true density ranges from 0.10 to 0.19 g/cc. Although manufacturers reported only ranges for true density, not size-dependent information, we could use the inverse linear relationship between size and true density initially found in this study. We estimated the true density to be 0.19 g/cc (maximum level) for the 30 μm size (10% of spheres) and 0.10 g/cc (maximum level) for the 105 μm size (90% of spheres). This result was consistent with the inverse linearity of the true density in Fig. 9A. By further substituting Eq. (5) into Eq. (3), an equation for the collapse pressure as a function of microsphere size can be derived (Fig. 9C). To improve the accuracy, we chose COMSOL Multiphysics (COMSOL Inc., Burlington, MA, USA) to simulate the collapse pressure to the sphere (Fig. 9D, E). The simulation measured the displacement when pressure was applied to a microsphere. The pressure followed a Gaussian distribution along the r-axis and was applied to all surfaces of the microsphere wall, and the point of contact with the bottom surface was fixed. To find the collapse pressure, the proportional limit, which is the point at which the linearity is lost, was obtained. The stationary study was used while increasing the applied pressure, which is mainly used to obtain the yield point (collapse pressure) of brittle materials, and it was obtained from the pressure–displacement curve, not the stress–strain curve for intuitive analysis (marked as B and C in Fig. S4A). For brittle materials, the proportional limit means the pressure point right before rupture [86]. When we plotted the proportional limits for each size, it showed an excellently matched trend with the derived equations (Fig. 9C). The fact that collapse pressure measurement study using high-frequency ultrasound showed the same trend also supports this graph [52]. This trend is also the same in other studies [52]. Therefore, we determined from the collapse pressures measured at 20 and 25 MHz that the true density and radius ratio vary with size, allowing us to estimate the collapse pressure characteristics at smaller sizes of HGMs used (P_{all}).

3.6. Application to a small HGM at 40 MHz

The collapse pressure was then measured at 40 MHz to demonstrate that the proposed measurement method can be applied to smaller microspheres. Each smaller microsphere was ruptured, and the acoustic pressure was measured using the curve for P_{all} . Because the calculated lateral resolution was 21 μm, we investigated microspheres in the 34–48-μm range, which was approximately 15 μm larger, as at other

frequencies. The recorded HGM size was 38 μm (Fig. 10A, Video S4). As the voltage was increased, partial and complete ruptures were observed at 21.1 and 21.5 V_{pp}, respectively.

We measured the acoustic pressure characteristics of the 40 MHz transducer. Because the beam characteristics of this transducer could not be accurately measured owing to the spatial averaging effect of the hydrophone [74,76], we solved this problem by measuring how much acoustic pressure was applied to the size of the HGM, not the acoustic pressure that the transducer radiates. We obtained experimentally threshold data of applied voltage at 18.7, 18.0, 15.9, 15.2, and 15.1 V_{pp} at 34–36, 37–39, 40–42, 43–45, and 46–48 μm, respectively (Fig. 10B). From the P_{all} curve, we found that the pressures at 35, 38, 41, 44, and 47 μm were 5.23, 5.03, 4.83, 4.63, and 4.44 MPa, respectively (Table S5). Using these values, we plotted the acoustic pressure as a function of applied voltage and found that, with a moderate coefficient of determination, a 40 MHz transducer radiates 2.608 times more pressure than a 20 MHz transducer (Fig. 11). The linear regression results included five data sets (n = 48) and a point of convergence to zero (no acoustic pressure if no voltage is applied to the transducer). Therefore, we measured the collapse pressures of smaller microspheres at 40 MHz and obtained the acoustic pressure characteristics of a 40 MHz focused beam.

4. Conclusion

We demonstrated for the first time that an acoustic tweezer can be used to measure the collapse pressures of microspheres. To measure collapse pressure, single HGMs are trapped and their collapse pressures measured at different frequencies, following a method that had not been attempted in previous acoustic tweezer studies. Using SBAT, the range of microsphere size appropriate for trapping and rupturing at each frequency was determined and the collapse pressure was measured. The measured collapse pressure values were validated using hydrophone measurements and compared with manufacturer's data. This collapse pressure measurement method excludes factors other than acoustic pressure, e.g., cavitation and interaction between microspheres, by isolating single microspheres to enable more accurate measurement. We also determined the relationship between true density and microsphere size from the variation in collapse pressure based on microsphere size and used this relation to determine a collapse pressure relation P_{all} as a function of microsphere size. Using P_{all} , the collapse pressures of smaller HGMs and the acoustic pressure characteristics of a 40 MHz transducer were estimated; this was possible because high-resolution acoustic tweezers can selectively trap a single HGM and rupture the microsphere with pulses ranging from low (-1 MPa) to high pressures (1–5 MPa). These results suggest that this measurement tool can be applied to calibrate the acoustic pressures of high-frequency (>40 MHz) transducers, eliminating the error caused by the spatial averaging effect of a hydrophone.

The proposed method can be further used to understand the dynamics of ultrasound contrast agents, where the bubbles are very small—typically<10 μm in diameter—and therefore require very high frequencies exceeding 100 MHz to measure. The study in this paper could be viewed as an initial investigation for this application, as it showed that even smaller spheres could be measured. Contrast agent bubbles are also composed of polymer or lipid shells, which are not as robust as glass to external factors, making measurement error potentially more significant. As the collapse pressures measured using single contrast agent bubbles yield more accurate values than those obtained from previous studies, the use of the proposed approach would be an effective method for understanding bubble dynamics under high-frequency ultrasound.

The proposed method might also be used to measure the elastic properties of various cells. These are often measured using atomic force microscopy, which has high resolution but limited pressure. The acoustic tweezer-based trap and collapse method might be able to measure elastic properties of cells at higher pressures with compromised resolution. Despite numerous studies on the measurement of elastic properties using ultrasound, most of them involved low-resolution measurement at < 100 MHz [70,87]. Our next step is to implement the proposed method using a very high-frequency (above 100 MHz) acoustic tweezer to obtain more accurate elastic property values.

CRediT authorship contribution statement

Jinhee Yoo: Conceptualization, Methodology, Validation, Formal analysis, Investigation, Writing – original draft. **Hyunhee Kim:** Methodology, Software, Investigation, Writing – original draft. **Yeonggeun Kim:** Resources, Visualization. **Hae Gyun Lim:** Methodology, Supervision, Writing – review & editing. **Hyung Ham Kim:** Conceptualization, Methodology, Validation, Project administration, Funding acquisition, Writing – review & editing.

Declaration of Competing Interest

The authors declare that they have no known competing financial interests or personal relationships that could have appeared to influence the work reported in this paper.

Acknowledgements

This work was supported in part by the National Research Foundation of Korea (NRF) grant funded by the Ministry of Science and ICT (No. 2019R1A2C2010484 and 2021R1F1A1062979), in part by the Basic Science Research Program through the NRF funded by the Ministry of Education (No. 2020R1A6A1A03047902), and in part by the Korea Medical Device Development Fund grant funded by the Korea government (the Ministry of Science and ICT, the Ministry of Trade, Industry and Energy, the Ministry of Health & Welfare, the Ministry of Food and Drug Safety) (No. 9991007324).

Appendix A. Supplementary data

Supplementary data to this article can be found online at https://doi.org/10.1016/j.ultsonch.2021.105844.

References

[1] B.B. Goldberg, J.-B. Liu, F. Forsberg, Ultrasound contrast agents: A review, Ultrasound Med, Biol. 20 (4) (1994) 319–333, https://doi.org/10.1016/0301-5629(94)90001-9.
[2] P.M. Shankar, P.D. Krishna, V.L. Newhouse, Subharmonic backscattering from ultrasound contrast agents, J. Acoust. Soc. Am. 106 (4) (1999) 2104–2110, https://doi.org/10.1121/1.428142.
[3] F. Forsberg, W.T. Shi, C.R.B. Merritt, Q. Dai, M. Solcova, B.B. Goldberg, On the Usefulness of the Mechanical Index Displayed on Clinical Ultrasound Scanners for Predicting Contrast Microbubble Destruction, J. Ultrasound Med. 24 (2005) 443–450, https://doi.org/10.7863/jum.2005.24.4.443.
[4] D.L. Miller, R.M. Thomas, Ultrasound contrast agents nucleate inertial cavitation in vitro, Ultrasound Med. Biol. 21 (8) (1995) 1059–1065, https://doi.org/10.1016/0301-5629(95)93252-U.
[5] R.W. Bourdeau, A. Lee-Gosselin, A. Lakshmanan, A. Farhadi, S.R. Kumar, S.P. Nety, M.G. Shapiro, Acoustic reporter genes for noninvasive imaging of microorganisms in mammalian hosts, Nature. 553 (7686) (2018) 86–90, https://doi.org/10.1038/nature25021.
[6] K. Ferrara, R. Pollard, M. Borden, Ultrasound microbubble contrast agents: Fundamentals and application to gene and drug delivery, Annu. Rev. Biomed. Eng. 9 (1) (2007) 415–447, https://doi.org/10.1146/annurev.bioeng.8.061505.095852.
[7] S.B. Barnett, G.R. Ter Haar, M.C. Ziskin, H.-D. Rott, F.A. Duck, K. Maeda, International recommendations and guidelines for the safe use of diagnostic ultrasound in medicine, Ultrasound Med. Biol. 26 (3) (2000) 355–366, https://doi.org/10.1016/S0301-5629(00)00204-0.
[8] D.L. Miller, C. Dou, Induction of Apoptosis in Sonoporation and Ultrasonic Gene Transfer, Ultrasound Med. Biol. 35 (1) (2009) 144–154, https://doi.org/10.1016/j.ultrasmedbio.2008.06.007.
[9] D.L. Miller, R.A. Gies, Gas-body-based contrast agent enhances vascular bioeffects of 1.09 MHz ultrasound on mouse intestine, Ultrasound Med. Biol. 24 (8) (1998) 1201–1208, https://doi.org/10.1016/S0301-5629(98)00063-5.

[10] D.M. Skyba, R.J. Price, A.Z. Linka, T.C. Skalak, S. Kaul, Direct in vivo visualization of intravascular destruction of microbubbles by ultrasound and its local effects on tissue, Circulation. 98 (4) (1998) 290–293, https://doi.org/10.1161/01.CIR.98.4.290.

[11] G.R. ter Haar, Ultrasonic contrast agents: safety considerations reviewed, Eur. J. Radiol. 41 (3) (2002) 217–221, https://doi.org/10.1016/S0720-048X(01)00456-9.

[12] B.L. Helfield, E. Cherin, F.S. Foster, D.E. Goertz, Investigating the Subharmonic Response of Individual Phospholipid Encapsulated Microbubbles at High Frequencies: A Comparative Study of Five Agents, Ultrasound Med. Biol. 38 (5) (2012) 846–863, https://doi.org/10.1016/j.ultrasmedbio.2012.01.011.

[13] Q. Sun, H. Gao, G.B. Sukhorukov, A.F. Routh, Silver-Coated Colloidosomes as Carriers for an Anticancer Drug, ACS Appl. Mater. Interfaces. 9 (38) (2017) 32599–32606, https://doi.org/10.1021/acsami.7b1112810.1021/acsami.7b11128.s001.

[14] A.L. White, C. Langton, M.L. Wille, J. Hitchcock, O.J. Cayre, S. Biggs, I. Blakey, A. K. Whittaker, S. Rose, S. Puttick, Ultrasound-triggered release from metal shell microcapsules, J. Colloid Interface Sci. 554 (2019) 444–452, https://doi.org/10.1016/j.jcis.2019.07.020.

[15] J.L. Paris, C. Mannaris, M.V. Cabañas, R. Carlisle, M. Manzano, M. Vallet-Regí, C. C. Coussios, Ultrasound-mediated cavitation-enhanced extravasation of mesoporous silica nanoparticles for controlled-release drug delivery, Chem. Eng. J. 340 (2018) 2–8, https://doi.org/10.1016/j.cej.2017.12.051.

[16] B. Kutlu, N. Takach, E.M. Ozbayoglu, S.Z. Miska, M. Yu, C. Mata, Drilling fluid density and hydraulic drag reduction with glass bubble additives, J. Energy Resour. Technol. Trans. ASME. 139 (2017) 1–11, https://doi.org/10.1115/1.4036540.

[17] J.-D. Kim, J.-H. Kim, J.-H. Ahn, J.-M. Lee, Glass bubble reinforced polyurethane foams with high mechanical strength for cryogenic temperature insulation, J. Appl. Polym. Sci. 138 (12) (2021) 50060, https://doi.org/10.1002/app.v138.1210.1002/app.50060.

[18] Y. Tao, S. Hinduja, R. Heinemann, A. Gomes, P.J. Bártolo, A study of physico-mechanical properties of hollow glass bubble, jute fibre and rubber powder reinforced polypropylene compounds with and without mucell® technology for lightweight applications, Polymers (Basel). 12 (2020) 1–13, https://doi.org/10.3390/polym12112664.

[19] J. DeCaprio, T.O. Kohl, Lysing Yeast Cells with Glass Beads for Immunoprecipitation, Cold Spring Harb. Protoc. 2020 (2020) 477–481, https://doi.org/10.1101/pdb.prot098590.

[20] C.-H. Hsu, C. Chen, D. Irimia, M. Toner, Fast sorting of CD4+ T cells from whole blood using glass microbubbles, Technology. 03 (01) (2015) 38–44, https://doi.org/10.1142/S2339547815500016.

[21] D.E. Goertz, D.A. Christopher, J.L. Yu, R.S. Kerbel, P.N. Burns, F.S. Foster, High-frequency color flow imaging of the microcirculation, Ultrasound Med. Biol. 26 (1) (2000) 63–71, https://doi.org/10.1016/S0301-5629(99)00101-5.

[22] M.R. Lowerison, C. Huang, Y. Kim, F. Lucien, S. Chen, P. Song, In Vivo Confocal Imaging of Fluorescently Labeled Microbubbles: Implications for Ultrasound Localization Microscopy, IEEE Trans. Ultrason. Ferroelectr. Freq. Control. 67 (9) (2020) 1811–1819, https://doi.org/10.1109/TUFFC.5810.1109/TUFFC.2020.298815910.1109/TUFFC.2020.2988159/mm110.1109/TUFFC.2020.2988159/mm2.

[23] Y. Sun, D.E. Kruse, P.A. Dayton, K.W. Ferrara, High-frequency dynamics of ultrasound contrast agents, IEEE Trans. Ultrason. Ferroelectr. Freq. Control. 52 (2005) 1981–1991, https://doi.org/10.1109/tuffc.2005.1561667.

[24] M. Piskunowicz, A. Sridharan, L. Poznick, E. Silvestro, M. Hwang, Optimization of Mechanical Indices for Clinical Contrast-Enhanced Ultrasound, J. Ultrasound Med. (2020) 1–8, https://doi.org/10.1002/jum.15578.

[25] M.M. Mahmud, X. Wu, J.L. Sanders, A.O. Biliroglu, O.J. Adelegan, I.G. Newsome, F.Y. Yamaner, P.A. Dayton, O. Oralkan, An Improved CMUT Structure Enabling Release and Collapse of the Plate in the Same Tx/Rx Cycle for Dual-Frequency Acoustic Angiography, IEEE Trans. Ultrason. Ferroelectr. Freq. Control. 67 (11) (2020) 2291–2302, https://doi.org/10.1109/TUFFC.5810.1109/TUFFC.2020.3001221.

[26] J.P. Christiansen, B.A. French, A.L. Klibanov, S. Kaul, J.R. Lindner, Targeted tissue transfection with ultrasound destruction of plasmid-bearing cationic microbubbles, Ultrasound Med. Biol. 29 (12) (2003) 1759–1767, https://doi.org/10.1016/S0301-5629(03)00976-1.

[27] S. Yoon, M.G. Kim, C.T. Chiu, J.Y. Hwang, H.H. Kim, Y. Wang, K.K. Shung, Direct and sustained intracellular delivery of exogenous molecules using acoustic-transfection with high frequency ultrasound, Sci. Rep. 6 (2016) 1–11, https://doi.org/10.1038/srep20477.

[28] S. Yoon, P. Wang, Q. Peng, Y. Wang, K.K. Shung, Acoustic-transfection for genomic manipulation of single-cells using high frequency ultrasound, Sci. Rep. 7 (2017) 1–11, https://doi.org/10.1038/s41598-017-05722-1.

[29] W.-S. Chen, T.J. Matula, A.A. Brayman, L.A. Crum, A comparison of the fragmentation thresholds and inertial cavitation doses of different ultrasound contrast agents, J. Acoust. Soc. Am. 113 (1) (2003) 643–651, https://doi.org/10.1121/1.1529667.

[30] C.C. Coussios, R.A. Roy, Applications of acoustics and cavitation to noninvasive therapy and drug delivery, Annu. Rev. Fluid Mech. 40 (1) (2008) 395–420, https://doi.org/10.1146/fluid.2008.40.issue-110.1146/annurev.fluid.40.111406.102116.

[31] G.A. Husseini, M.A. Diaz de la Rosa, E.S. Richardson, D.A. Christensen, W.G. Pitt, The role of cavitation in acoustically activated drug delivery, J. Control. Release. 107 (2) (2005) 253–261, https://doi.org/10.1016/j.jconrel.2005.06.015.

[32] C.C. Church, Frequency, pulse length, and the mechanical index, Acoust. Res. Lett, Online. 6 (3) (2005) 162–168, https://doi.org/10.1121/1.1901757.

[33] A. Jamburidze, M. De Corato, A. Huerre, A. Pommella, V. Garbin, High-frequency linear rheology of hydrogels probed by ultrasound-driven microbubble dynamics, Soft Matter. 13 (21) (2017) 3946–3953, https://doi.org/10.1039/C6SM02810A.

[34] A. Prosperetti, A generalization of the Rayleigh-Plesset equation of bubble dynamics, Phys. Fluids. 25 (1982) 409–410, https://doi.org/10.1063/1.863775.

[35] S.-L. Fok, D.J. Allwright, Buckling of a spherical shell embedded in an elastic medium loaded by a far-field hydrostatic pressure, J. Strain Anal. Eng. Des. 36 (6) (2001) 535–544, https://doi.org/10.1243/0309324011514692.

[36] H. Wu, C. Zhou, Z. Pu, X. Lai, H. Yu, D. Li, Experimental investigation on the effects of the standoff distance and the initial radius on the dynamics of a single bubble near a rigid wall in an ultrasonic field, Ultrason. Sonochem. 68 (2020) 105197, https://doi.org/10.1016/j.ultsonch.2020.105197.

[37] Q. Yu, X. Ma, Z. Xu, J. Zhao, D. Wang, Z. Huang, Thermodynamic Effect of Single Bubble Near a Rigid Wall, Ultrason. Sonochem. 71 (2021) 105396, https://doi.org/10.1016/j.ultsonch.2020.105396.

[38] G. Huang, M. Zhang, X. Ma, Q. Chang, C. Zheng, B. Huang, Dynamic behavior of a single bubble between the free surface and rigid wall, Ultrason. Sonochem. 67 (2020) 105147, https://doi.org/10.1016/j.ultsonch.2020.105147.

[39] X. Ma, B. Huang, X. Zhao, Y. Wang, Q. Chang, S. Qiu, X. Fu, G. Wang, Comparisons of spark-charge bubble dynamics near the elastic and rigid boundaries, Ultrason. Sonochem. 43 (2018) 80–90, https://doi.org/10.1016/j.ultsonch.2018.01.005.

[40] A. Shima, The natural frequencies of two spherical bubbles oscillating in water, J. Fluids Eng. Trans. ASME. 93 (1971) 426–431, https://doi.org/10.1115/1.3425268.

[41] P.P. Chang, W.S. Chcn, P.D. Mourad, S.L. Poliachik, L.A. Crum, Thresholds for inertial cavitation in Albunex suspensions under pulsed ultrasound conditions, IEEE Trans. Ultrason. Ferroelectr. Freq. Control. 48 (2001) 161–170, https://doi.org/10.1109/58.895927.

[42] K. Yasui, J. Lee, T. Tuziuti, A. Towata, T. Kozuka, Y. Iida, Influence of the bubble-bubble interaction on destruction of encapsulated microbubbles under ultrasound, J. Acoust. Soc. Am. 126 (3) (2009) 973–982, https://doi.org/10.1121/1.3179677.

[43] J. Liang, X. Wang, J. Yang, L. Gong, Dynamics of two interacting bubbles in a nonspherical ultrasound field, Ultrasonics. 75 (2017) 58–62, https://doi.org/10.1016/j.ultras.2016.11.012.

[44] J. Luo, Z. Niu, Jet and Shock Wave from Collapse of Two Cavitation Bubbles, Sci. Rep. 9 (2019) 1–13, https://doi.org/10.1038/s41598-018-37868-x.

[45] S.W. Fong, D. Adhikari, E. Klaseboer, B.C. Khoo, Interactions of multiple spark-generated bubbles with phase differences, Exp. Fluids. 46 (4) (2009) 705–724, https://doi.org/10.1007/s00348-008-0603-4.

[46] N. Ochiai, J. Ishimoto, Numerical analysis of the effect of bubble distribution on multiple-bubble behavior, Ultrason. Sonochem. 61 (2020) 104818, https://doi.org/10.1016/j.ultsonch.2019.104818.

[47] A.Y. Ammi, R.O. Cleveland, J. Mamou, G.I. Wang, S.L. Bridal, W.D. O'Brien, Ultrasonic contrast agent shell rupture detected by inertial cavitation and rebound signals, IEEE Trans. Ultrason. Ferroelectr. Freq. Control. 53 (1) (2006) 126–136, https://doi.org/10.1109/TUFFC.2006.1588398.

[48] M. Gauthier, D.A. King, W.D. O'Brien, Influence of microbubble size on postexcitation collapse thresholds for single ultrasound contrast agents using double passive cavitation detection - [Letters], IEEE Trans. Ultrason. Ferroelectr. Freq. Control. 60 (5) (2013) 877–879, https://doi.org/10.1109/TUFFC.5810.1109/TUFFC.2013.2644.

[49] D.A. King, W.D. O'Brien, Quantitative analysis of ultrasound contrast agent postexcitation collapse, IEEE Trans. Ultrason. Ferroelectr. Freq. Control. 61 (2014) 1237–1241, https://doi.org/10.1109/TUFFC.2014.3023.

[50] J. Mamou, J.A. Ketterling, Subharmonic analysis using singular-value decomposition of ultrasound contrast agents, J. Acoust. Soc. Am. 125 (6) (2009) 4078–4091, https://doi.org/10.1121/1.3117384.

[51] P.V. Chitnis, P. Lee, J. Mamou, J.S. Allen, M. Böhmer, J.A. Ketterling, Rupture threshold characterization of polymer-shelled ultrasound contrast agents subjected to static overpressure, J. Appl. Phys. 109 (8) (2011) 084906, https://doi.org/10.1063/1.3565062.

[52] P.V. Chitnis, S. Koppolu, J. Mamou, C. Chlon, J.A. Ketterling, Influence of shell properties on high-frequency ultrasound imaging and drug delivery using polymer-shelled microbubbles, IEEE Trans. Ultrason. Ferroelectr. Freq. Control. 60 (1) (2013) 53–64, https://doi.org/10.1109/TUFFC.2013.2537.

[53] P.A. Quinto-Su, A microscopic steam engine implemented in an optical tweezer, Nat. Commun. 5 (2014) 1–7, https://doi.org/10.1038/ncomms6889.

[54] D. Baresch Correction for Baresch and Garbin, Acoustic trapping of microbubbles in complex environments and controlled payload release Proc. Natl. Acad. Sci. 117 2020 20969 20969 10.1073/pnas.2014821117.

[55] K.C. Neuman, A. Nagy, Single-molecule force spectroscopy: Optical tweezers, magnetic tweezers and atomic force microscopy, Nat. Methods. 5 (6) (2008) 491–505, https://doi.org/10.1038/nmeth.1218.

[56] H.u. Zhang, K.-K. Liu, Optical tweezers for single cells, J. R. Soc. Interface. 5 (24) (2008) 671–690, https://doi.org/10.1098/rsif.2008.0052.

[57] A. Ashkin, J.M. Dziedzic, Optical trapping and manipulation of viruses and bacteria, Science (80-.). 235 (1987) 1517–1520. https://doi.org/10.1126/science.3547653.

[58] H.G. Lim, Y. Li, M.-Y. Lin, C. Yoon, C. Lee, H. Jung, R.H. Chow, K.K. Shung, Calibration of Trapping Force on Cell-Size Objects From Ultrahigh-Frequency Single-Beam Acoustic Tweezer, IEEE Trans. Ultrason. Ferroelectr. Freq. Control. 63 (11) (2016) 1988–1995, https://doi.org/10.1109/TUFFC.2016.2600748.

[59] J. Lee, C. Lee, K.K. Shung, Calibration of sound forces in acoustic traps, IEEE Trans. Ultrason. Ferroelectr. Freq. Control. 57 (2010) 2305–2310, https://doi.org/10.1109/TUFFC.2010.1691.

[60] H.G. Lim, H.H. Kim, C. Yoon, Evaluation method for acoustic trapping performance by tracking motion of trapped microparticle, Jpn. J. Appl. Phys. 57 (5) (2018) 057202, https://doi.org/10.7567/JJAP.57.057202.
[61] Y. Li, C. Lee, K. Ho Lam, K. Kirk Shung, A simple method for evaluating the trapping performance of acoustic tweezers, Appl. Phys. Lett. 102 (8) (2013) 084102, https://doi.org/10.1063/1.479365410.1063/1.4793654.1.
[62] J.Y. Hwang, J. Kim, J.M. Park, C. Lee, H. Jung, J. Lee, K.K. Shung, Cell Deformation by Single-beam Acoustic Trapping: A Promising Tool for Measurements of Cell Mechanics, Sci. Rep. 6 (2016) 1–8, https://doi.org/10.1038/srep27238.
[63] H.G. Lim, K.K. Shung, Quantification of Inter-Erythrocyte Forces with Ultra-High Frequency (410 MHz) Single Beam Acoustic Tweezer, Ann. Biomed. Eng. 45 (9) (2017) 2174–2183, https://doi.org/10.1007/s10439-017-1863-z.
[64] K.H. Lam, Y. Li, Y. Li, H.G. Lim, Q. Zhou, K.K. Shung, Multifunctional single beam acoustic tweezer for non-invasive cell/organism manipulation and tissue imaging, Sci. Rep. 6 (2016) 1–7, https://doi.org/10.1038/srep37554.
[65] X. Ding, S.-C.-S. Lin, B. Kiraly, H. Yue, S. Li, I.-K. Chiang, J. Shi, S.J. Benkovic, T. J. Huang, On-chip manipulation of single microparticles, cells, and organisms using surface acoustic waves, Proc. Natl. Acad. Sci. U. S. A. 109 (28) (2012) 11105–11109, https://doi.org/10.1073/pnas.1209288109.
[66] X. Peng, W. He, F. Xin, G.M. Genin, T.J. Lu, Standing surface acoustic waves, and the mechanics of acoustic tweezer manipulation of eukaryotic cells, J. Mech. Phys. Solids. 145 (2020) 104134, https://doi.org/10.1016/j.jmps.2020.104134.
[67] A. Marzo, S.A. Seah, B.W. Drinkwater, D.R. Sahoo, B. Long, S. Subramanian, Holographic acoustic elements for manipulation of levitated objects, Nat. Commun. 6 (2015) 1–7, https://doi.org/10.1038/ncomms9661.
[68] S.T. Kang, C.K. Yeh, Potential-well model in acoustic tweezers, IEEE Trans. Ultrason. Ferroelectr. Freq. Control. 57 (2010) 1451–1459, https://doi.org/10.1109/TUFFC.2010.1564.
[69] X. Chen, K.H. Lam, R. Chen, Z. Chen, P. Yu, Z. Chen, K.K. Shung, Q. Zhou, An adjustable multi-scale single beam acoustic tweezers based on ultrahigh frequency ultrasonic transducer, Biotechnol. Bioeng. 114 (11) (2017) 2637–2647, https://doi.org/10.1002/bit.v114.1110.1002/bit.26365.
[70] H.G. Lim, H.-C. Liu, C.W. Yoon, H. Jung, M.G. Kim, C. Yoon, H.H. Kim, K.K. Shung, Investigation of cell mechanics using single-beam acoustic tweezers as a versatile tool for the diagnosis and treatment of highly invasive breast cancer cell lines: an in vitro study, Microsystems Nanoeng. 6 (1) (2020), https://doi.org/10.1038/s41378-020-0150-6.
[71] H.G. Lim, H.H. Kim, C. Yoon, K.K. Shung, A one-sided acoustic trap for cell immobilization using 30-MHz array transducer, IEEE Trans. Ultrason. Ferroelectr. Freq. Control. 67 (1) (2020) 167–172, https://doi.org/10.1109/TUFFC.5810.1109/TUFFC.2019.2940239.
[72] Z. Li, D. Wang, C. Fei, Z. Qiu, C. Hou, R. Wu, D.i. Li, Q. Zhang, D. Chen, Z. Chen, W. Feng, Y. Yang, The Forbidden Band and Size Selectivity of Acoustic Radiation Force Trapping, IScience. 24 (1) (2021) 101988, https://doi.org/10.1016/j.isci.2020.101988.
[73] J.A. Jensen, Simulation of advanced ultrasound systems using field II, 2004 2nd IEEE Int Symp. Biomed. Imaging Macro to Nano. 1 (2004) (2004) 636–639, https://doi.org/10.1109/isbi.2004.1398618.
[74] R.C. Preston, D.R. Bacon, A.J. Livett, K. Rajendran, PVDF membrane hydrophone performance properties and their relevance to the measurement of the acoustic output of medical ultrasonic equipment, J. Phys. E. 16 (8) (1983) 786–796, https://doi.org/10.1088/0022-3735/16/8/019.
[75] B. Zeqiri, A.D. Bond, The influence of waveform distortion on hydrophone spatial-averaging corrections—Theory and measurement, J. Acoust. Soc. Am. 92 (4) (1992) 1809–1821, https://doi.org/10.1121/1.403837.
[76] K.A. Wear, Hydrophone Spatial Averaging Correction for Acoustic Exposure Measurements from Arrays-Part I: Theory and Impact on Diagnostic Safety Indexes, IEEE Trans. Ultrason. Ferroelectr. Freq. Control. 68 (3) (2021) 358–375, https://doi.org/10.1109/TUFFC.5810.1109/TUFFC.2020.3037946.
[77] B. Roy, A. Ramaiya, E. Schäffer, Determination of pitch rotation in a spherical birefringent microparticle, J. Opt. 20 (3) (2018) 035603, https://doi.org/10.1088/2040-8986/aaa9e4.
[78] Y. Lu, J.D. Carroll, K.N. Long, R. Long, Failure of brittle micro-spherical shells embedded in elastomer matrix under indentation, Compos. Part B Eng. 173 (2019) 106870, https://doi.org/10.1016/j.compositesb:2019.05.081.
[79] H.T. O'Neil, Theory of Focusing Radiators, J. Acoust. Soc. Am. 21 (5) (1949) 516–526, https://doi.org/10.1121/1.1906542.
[80] D. Cathignol, O.A. Sapozhnikov, Y. Theillère, Comparison of acoustic fields radiated from piezoceramic and piezocomposite focused radiators, J. Acoust. Soc. Am. 105 (5) (1999) 2612–2617, https://doi.org/10.1121/1.426877.
[81] L. Hoff, P.C. Sontum, J.M. Hovem, Oscillations of polymeric microbubbles: Effect of the encapsulating shell, J. Acoust. Soc. Am. 107 (4) (2000) 2272–2280, https://doi.org/10.1121/1.428557.
[82] B.H. Rutz, J.C. Berg, A review of the feasibility of lightening structural polymeric composites with voids without compromising mechanical properties, Adv. Colloid Interface Sci. 160 (1-2) (2010) 56–75, https://doi.org/10.1016/j.cis.2010.07.005.
[83] C. Swetha, R. Kumar, Quasi-static uni-axial compression behaviour of hollow glass microspheres/epoxy based syntactic foams, Mater. Des. 32 (8-9) (2011) 4152–4163, https://doi.org/10.1016/j.matdes.2011.04.058.
[84] B. Dillinger, D. Clark, C. Suchicital, G. Wicks, Crush strength analysis of hollow glass microspheres, Ceram. Eng. Sci. Proc. 38 (2018) 11–26, https://doi.org/10.1002/9781119474678.ch2.
[85] S. Ren, X. Li, X. Zhang, X. Xu, X. Dong, J. Liu, H. Du, A. Guo, Mechanical properties and high-temperature resistance of the hollow glass microspheres/borosilicate glass composite with different particle size, J. Alloys Compd. 722 (2017) 321–329, https://doi.org/10.1016/j.jallcom.2017.06.092.
[86] H.J. Leamy, T.T. Wang, H.S. Chen, Plastic flow and fracture of metallic glass, Metall. Trans. 3 (1972) 699–708, https://doi.org/10.1007/BF02642754.
[87] H.C. Liu, E.J. Gang, H.N. Kim, H.G. Lim, H. Jung, R. Chen, H. Abdel-Azim, K. K. Shung, Y.M. Kim, Characterizing Deformability of Drug Resistant Patient-Derived Acute Lymphoblastic Leukemia (ALL) Cells Using Acoustic Tweezers, Sci. Rep. 8 (2018) 1–10, https://doi.org/10.1038/s41598-018-34024-3.